RESEARCH ARTICLE
SPACE PHYSICS

Earth and Planetary Physics
4: 619–626, 2020
doi: 10.26464/epp2020066

The semiannual variation of transpolar arc incidence and its relationship to the Russell–McPherron effect

Tao Tang[1], Jun Yang[1], QuanQi Shi[1]*, AnMin Tian[1], Shi-Chen Bai[1], Alexander William Degeling[1], SuiYan Fu[2], JingXian Liu[1], Tong Shao[1], and ZeYuan Sun[1]

[1]Shandong Key Laboratory of Optical Astronomy and Solar-Terrestrial Environment, School of Space Science and Physics, Institute of Space Sciences, Shandong University, Weihai Shandong 264209, China;

[2]Institute of Space Physics and Applied Technology, Peking University, Beijing 100871, China

Key Points:

- A semiannual variation in the incidence of TPAs is found via statistical analysis of long-term TPA observations
- The intensity and occurrence rate of the northward IMF also exhibit a similar seasonal variation
- The R-M effect may explain the incidence and magnitude of the northward IMF, which in turn affects the semiannual variation of TPA incidence

Citation: Tang, T., Yang, J., Shi, Q. Q., Tian, A. M., Bai, S.-C., Degeling, A. W., Fu, S. Y., Liu, J. X., Shao, T. and Sun, Z. Y. (2020). The semiannual variation of transpolar arc incidence and its relationship to the Russell–McPherron effect. *Earth Planet. Phys.*, *4*(6), 619–626. http://doi.org/10.26464/epp2020066

Abstract: Earth's aurora is a luminescent phenomenon generated by the interaction between magnetospheric precipitating particles and the upper atmosphere; it plays an important role in magnetosphere–ionosphere (M-I) coupling. The transpolar arc (TPA) is a discrete auroral arc distributed in the noon-midnight direction poleward of the auroral oval and connects the dayside to the nightside sectors of the auroral oval. Studying the seasonal variation of TPA events can help us better understand the long-term variation of the interaction between the solar wind, the magnetosphere, and M-I coupling. However, a statistical study of the seasonal variation of TPA incidence has not previously been carried out. In this paper, we have identified 532 TPA events from the IMAGE database (2000–2005) and the Polar database (1996–2002), and calculated the incidence of TPA events for different months. We find a semiannual variation in TPA incidence. Clear peaks in the incidence of TPAs occur in March and September; a less pronounced peak appears in November. We also examine seasonal variation in the northward interplanetary magnetic field (IMF) over the same time period. The intensity and occurrence rate of the northward IMF exhibit patterns similar to that of the TPA incidence. Having studied IMF B_z before TPA onset, we find that strong and steady northward IMF conditions are favorable for TPA formation. We suggest that the semiannual variation observed in TPA incidence may be related to the Russell–McPherron (R-M) effect due to the projection effect of the IMF B_y under northward IMF conditions.

Keywords: transpolar arc incidence; interplanetary magnetic field; Russell–McPherron effect; semiannual variation

1. Introduction

Earth's aurora occurs when magnetospheric particles (electrons and protons) precipitate along magnetic field lines into the ionosphere and collide with neutral atomic or molecular species, causing spectral line emission (and ionization) (Rees, 1963; Shi QQ et al., 2009, 2013). The brightness of the aurora is not constant and may fluctuate momentarily (Zhou XZ et al., 2012). Previous studies have recorded the geographical positions of the aurora observed at night and have found that the center of the oval structure is roughly at the geomagnetic pole (Feldstein and Starkov, 1967; Frank et al., 1982; Yokoyama et al., 1998).

The transpolar arc (TPA), also known as "Sun-aligned auroral arc" and "theta aurora", is a discrete auroral arc distributed in the noon-midnight direction poleward of the auroral oval; it usually connects the dayside and nightside sectors of the auroral oval (Frank et al., 1986). TPAs, first reported by Frank et al. (1982), appear under northward interplanetary magnetic field (IMF) conditions. They are more likely to be observed in the dayside of the polar cap region (Lassen and Danielsen, 1989); however, in the northern and southern hemispheres, branches of a TPA originating from the dayside and nightside can be observed simultaneously (Craven et al., 1991; Eriksson et al., 2005; Mailyan et al., 2015; Carter et al., 2017).

Previous studies suggest that TPAs may form on closed magnetic field lines (Peterson and Shelley, 1984; Frank et al., 1986; Tanaka et al., 2004), while other suggest that TPAs occur on open magnetic field lines (Gussenhoven and Mullen, 1989). The generation and evolution of TPAs are related to the polarity and strength of the IMF. Therefore, the incidence of TPAs should also be related. Sev-

Correspondence to: Q. Q. Shi, sqq@sdu.edu.cn
Received 10 MAY 2020; Accepted 13 JUL 2020.
Accepted article online 18 AUG 2020.

eral models have been proposed to explain the generation of TPAs under different IMF conditions (Kullen, 2000; Milan et al., 2005). Previous statistical studies have shown that TPAs are more likely to occur under northward IMF conditions with strong northward B_z components (Berkey et al., 1976; Gussenhoven, 1982; Kullen et al., 2002); that TPAs generally occur during quiet times under northward IMF conditions, and disappear after substorm onset (Hultqvist, 1974); that shapes and positions of TPAs may change or remain constant over time (Kullen, 2012); and that the strength and variation of the IMF B_y directly affects the position and motion of the TPA (Frank et al., 1985; Kullen et al., 2002; Fear and Milan, 2012).

It is known that both solar wind disturbance and IMF conditions have important influence on geomagnetic activities (Zong Q-G et al., 2009, 2012; Zhang XY et al., 2010; Yue C et al., 2010, 2011; Yue C and Zong QG, 2011). The IMF conditions relative to Earth's dipole tilt significantly affect geomagnetic activity, which exhibits semiannual variation, peaks in March and September, and reaches minima in June and December (Russell and McPherron, 1973; Cliver et al., 2000, 2002). The Russell–McPherron (R-M) effect (Russell and McPherron, 1973) is the prevailing hypothesis to explain this variation. The R-M effect considers that the seasonal variation of the intensity of the negative IMF B_z in GSM coordinates is the key parameter that explains the semiannual variation of the geomagnetic activity. According to the R-M effect, the amplitude of the IMF B_z component has semiannual variation which reaches its maximum near the Spring and Autumn Equinoxes and reaches its minimum near the summer and the winter solstices. Given that the generation of the TPA is affected by IMF strength, while IMF strength is modulated by the Russell and McPherron (R-M) effect, it is logical to expect that the TPA incidence might also have a semi-annual variation due to the R-M effect (Russell and McPherron, 1973).

TPAs are the energy release process of the magnetosphere under northward IMF conditions; as such, they can be considered as counterparts of the substorm under southward IMF conditions (Crooker, 1992). The long-term variation of mass transport and energy dissipation under southward IMF conditions have been discussed extensively (Liou et al., 2001). However, no statistical study of the seasonal variation of TPA incidence, which reflects the long-term variation of mass transport and energy dissipation under northward IMF conditions, has yet been carried out. In this paper, we investigate the seasonal variation of the incidence of TPAs and correlate these events to the IMF conditions at the time of each. In addition, we discuss the mechanisms proposed to have causal relationship to the seasonal variation in the incidence of TPAs.

2. Data

The Imager for Magnetopause-to-Aurora Global Exploration (IMAGE) spacecraft was launched in March 2000 and operated until December 2005. The spacecraft was able to capture images of the entire auroral oval. The Wideband Imaging Camera (WIC) onboard the IMAGE spacecraft captured auroral images with a size of 256×256 pixels and a spatial resolution of about 100 km at apogee (Mende et al., 2000a, b). The camera was sensitive to the spectral wavelength band from 140 to 190 nm (Lyman–Birge–Hopfield) and captured images every 2 minutes (Mende et al., 2000c). In this paper, we use IMAGE satellite data from 2000–2003 (imaging in the northern hemisphere) and 2003–2005 (imaging in the southern hemisphere), with a small amount of imaging data in both hemispheres in 2003.

The Polar spacecraft was launched in 1996 and operated until 2008. The satellite was placed in an elliptical orbit with an inclination of about 86° and an orbital period of 17 hours. The Polar UVI (Ultraviolet Imager) had an 8° field of view, capturing images approximately every half minute (Torr et al., 1995). In this paper, we use data from 1996–2002 (in Northern Hemisphere Imaging).

To study the seasonal variation of the northward IMF ($B_z > 0$), we use IMF data from the OMNI database with 1 hour resolution (in order to calculate monthly ensemble averages of IMF B_z for the years of the aurora data that we use, 1996 to 2005) and 1 minute resolution (in order to calculate the characteristics of IMF values prior to each TPA event).

3. Observation

3.1 TPA Incidence

This study calculates the incidence of TPAs in every month by two different methods, duration of events and number of events:

(1) The ratio between the total occurrence time of TPAs T_{TPA} and the total occurrence time of aurora T_{A} in a given month is defined as the occurrence rate P of TPAs for that month:

$$P = \frac{T_{\mathrm{TPA}}}{T_{\mathrm{A}}}. \tag{1}$$

(2) The ratio between the number of TPA events N_{TPA} (instead of total TPA occurrence time) to total aurora time T_{A} in a given month is defined to be occurrence rate R for that month:

$$R = \frac{N_{\mathrm{TPA}}}{T_{\mathrm{A}}}. \tag{2}$$

To calculate the uncertainty in TPA incidence, the statistical uncertainties from multiple observations of T_{TPA} and T_{A} are calculated using the definition of sample standard deviation given in Equation (3), where X_i, is a set of N observations with mean $\bar{X}$:

$$\sigma_X = \sqrt{\frac{1}{N-1}\sum (X_i - \bar{X})^2}. \tag{3}$$

The uncertainty in N_{TPA} is given by the value of its square root, based on counting statistics. Then the uncertainty in TPA incidence is obtained by using the law of error propagation.

We record the time periods during which a clear portion of the auroral oval is observed, and aggregate these times to find the total time of the aurora per month. Similarly, we choose the intervals during which a TPA occurs and aggregate these times to calculate the total time of TPA presence per month. The start/end time of each period is determined by the time when the auroral oval or TPA appears/disappears in the satellite images.

We define the start/end times of the auroral oval when a portion of the auroral oval starts to be visible/invisible in the satellite image that spans a range in magnetic local time (MLT) of greater than 12 hours (i.e. greater than 50% of the entire oval). To rule out

effects caused by the duration of TPAs, we record only the number of the TPA events that last longer than half an hour, and we treat two consecutive TPA events as one event if the two events appear at the same location and the time interval between them is less than half an hour. We exclude the time periods from statistics whenever the aurora image is incomplete, missing, or fuzzy, and we cannot thus be certain that a TPA has occurred. Dayglow strongly affects the polar imaging in both hemispheres, so during these times we use the auroral images in which the contamination caused by dayglow has been reduced using an image processing technique (Li X et al., 2004). Figure 1 shows typical examples of auroral ovals and TPA events. The color indicates the intensity of the aurora. The extreme brightness of the images on the dayside is caused by dayglow. From Figure 1(a–c), we can clearly see the evolution of the "glowing circle" between magnetic latitudes of 60° and 80°; this is the auroral oval. Using the criteria given above, the start time of the auroral oval can be determined as 11:02:17 in Figure 1a. A TPA case starting at 12:24:01 UT and ending at 16:00:47 UT is shown in Figure 1(d–i). It reaches its peak intensity at 15:17:50 UT in Figure 1g, when the TPA is shown to be crossing the entire auroral oval in the dusk side.

Based on the statistical criteria listed above, we identified 532 TPA events in total. Among these events, 437 occured in the northern hemisphere and 95 events in the southern hemisphere. A total of 278 events come from the IMAGE satellite database and 254 events from the Polar satellite database. The TPA events in the Southern Hemisphere were all observed by IMAGE. Since the IMAGE and Polar satellites were imaging in the southern hemisphere only during the final working period, the data volume in the southern hemisphere is relatively small. Therefore, the segregation of TPA incidence to the northern and southern hemispheres is not considered in this study. The number and total time of the TPA events and the total time of the auroral oval in the different

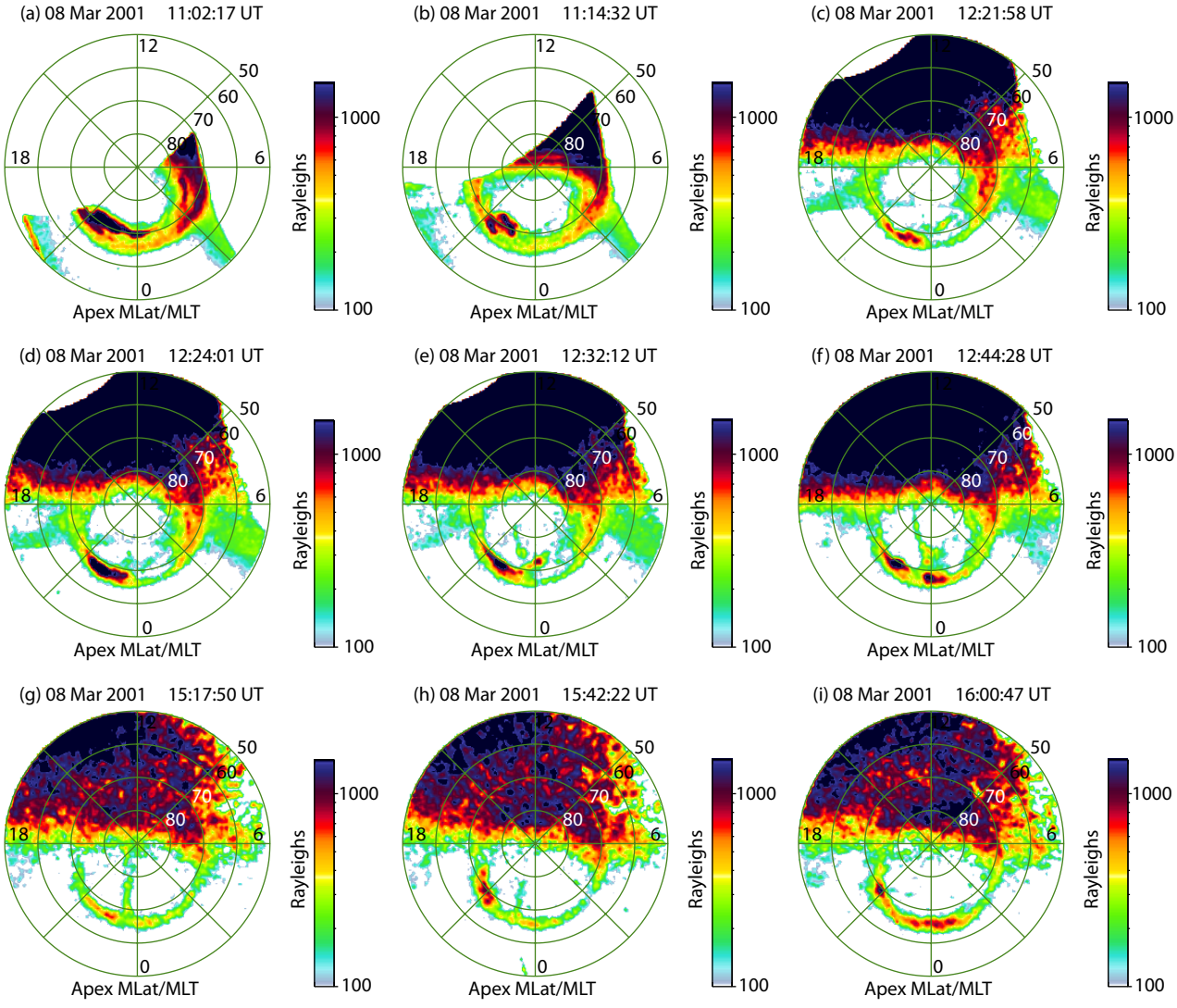

Figure 1. Nine selected snapshots of the auroral oval and TPAs in the Northern Hemisphere observed by the IMAGE satellite on 8 March 2001. Pictures are arranged in chronological order. Concentric circles from the outside to the inside mark magnetic latitudes of 50° to 80°. The bottom, right, top, and left sides of each plot show 0, 6, 12, and 18 h in magnetic local time (MLT), respectively. The colorbars shown on the right side of these images show the intensity of the aurora in Rayleigh units. The area above the lines connecting 06:00 to 18:00 MLT is dayglow. Panels (a–c) show the background auroral oval before the TPA event; Panels (d–i) show the TPA event.

Table 1. Total time of aurora occurrence, and total time and number of TPA events, in each month.

	Jan.	Feb.	Mar.	Apr.	May.	Jun.	Jul.	Aug.	Sep.	Oct.	Nov.	Dec.
Total time of aurora	145.351	147.538	124.731	90.288	151.076	169.177	164.137	182.005	162.782	94.437	154.180	166.133
Total time of TPA	2.190	2.872	3.650	1.148	1.784	1.898	2.177	2.551	4.405	1.699	3.661	2.437
Total number of TPA	39	55	62	21	31	40	43	47	64	28	60	42
Total time of aurora in northern hemisphere	122.943	123.113	104.927	86.076	134.078	138.894	145.038	147.249	124.071	86.887	123.869	142.387
Total time of TPA in northern hemisphere	2.080	2.550	2.967	1.015	1.468	1.385	1.810	1.655	2.867	1.648	3.242	2.163
Total number of TPA in northern hemisphere	35	49	52	19	26	29	34	32	46	27	51	37
Total time of aurora in southern hemisphere	22.408	24.424	19.804	4.212	16.999	30.283	19.099	34.756	38.711	7.550	30.311	23.746
Total time of TPA in southern hemisphere	0.109	0.322	0.683	0.133	0.316	0.513	0.368	0.896	1.538	0.052	0.419	0.275
Total number of TPA in southern hemisphere	4	6	10	2	5	11	9	15	18	1	9	5

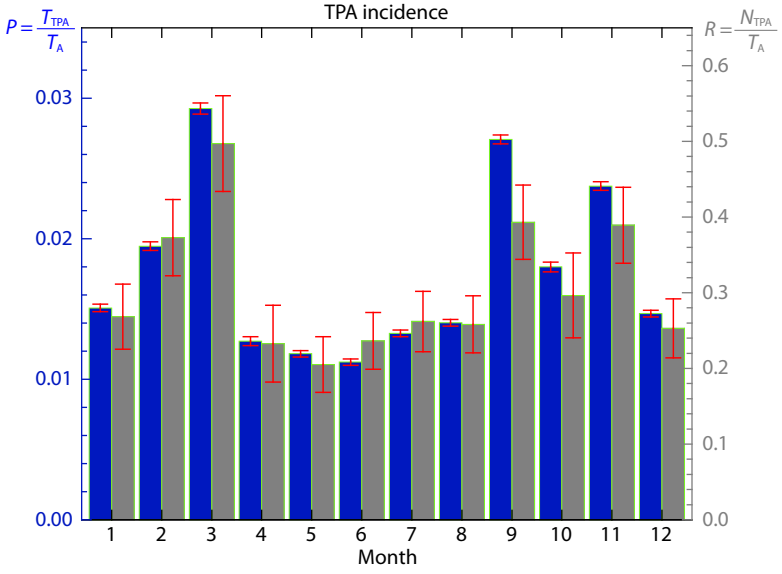

Figure 2. Based on IMAGE and Polar satellite aurora data (all data in both hemispheres), the TPA incidence is calculated according to Equation (1) and Equation (2).

hemispheres in each month are shown in Table 1.

Figure 2 shows the monthly occurrence rate of observed TPAs in both hemispheres, calculated according to Equations (1) and (2). The error bar is added on the histogram. Both of these results show similar trends. Clearly significant peaks in the incidence of TPAs occur in March and September. A somewhat less prominent peak appears to occur in November. Significant troughs appear in December/January, and May/June. The data also show a weak local trough in October (separating the peaks in September and November). These results clearly show that the incidence of TPAs has a significant semiannual variation.

3.2 IMF B_z Observation

Figure 3 presents the variation of IMF B_z (B_z> 0 in GSM) in each month, calculated from OMNI 1 h resolution solar wind data from 1996 to 2005. Seasonal and diurnal variations of IMF B_z are shown in Figure 3a and Figure 3b. The horizontal axis represents the seasonal variation and the vertical axis represents the diurnal variation. The B_z mean (Figure 3a) and the probability of B_z > 2 nT (Figure 3b) are calculated in a 24 × 24 grid, smoothed by means of 3 × 3 averaging. As can be seen from Figure 3a and Figure 3b, the observation of B_z is in good agreement with the predicted result of the R-M effect (Russell and McPherron, 1973; Zhao H and Zong QG, 2012; Bai et al., 2018), which suggests that the R-M effect can also predict the semiannual variation of the northward IMF. Figure 3c presents a histogram of the average value of the northward IMF B_z data for each month. Figure 3d is a histogram of the probability of greater than 2 nT in the northward IMF B_z data for each month. The reason for using the 2 nT threshold in Figure 3b

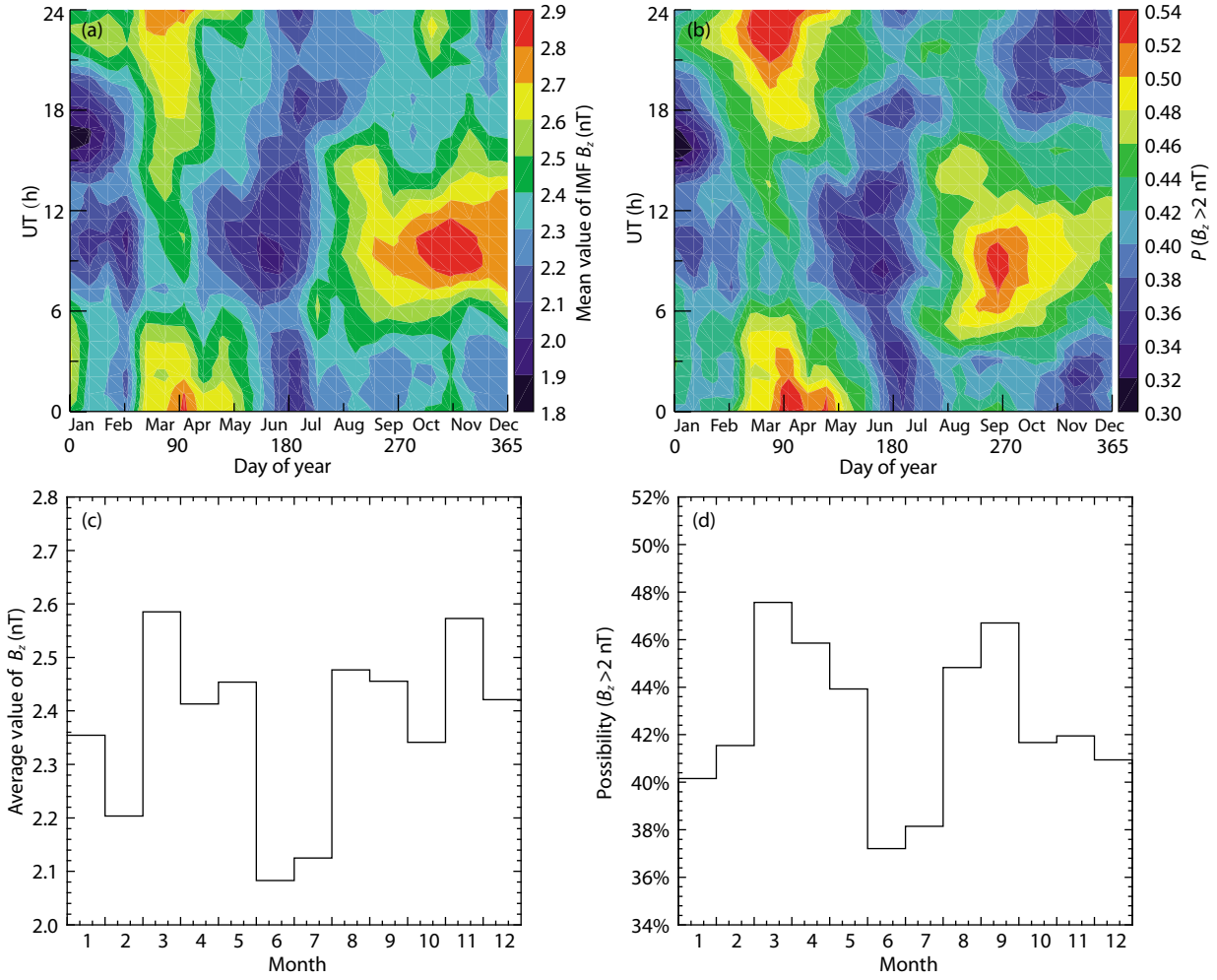

Figure 3. (a) Seasonal variation and diurnal variation of the mean value of the northward IMF B_z in the statistical year. (b) Seasonal variation and diurnal variation of the probability of a northward IMF $B_z > 2$ nT in the statistical year. (c) The mean value of the northward IMF B_z in each month. (d) The probability of northward IMF $B_z > 2$ nT in each month.

and Figure 3d is found in the results shown in Figure 4a, which will be discussed later. Figure 3d shows a clear semiannual variation trend, with peaks in March and September and valleys in December/January and June. From Figure 3c, we can see a vague semiannual variation trend, while there seems to be another peak in November, consistent with the apparent November peak in TPA incidence seen in Figure 2.

Previous studies considering the time delay between TPA observations and corresponding IMF observations have shown that the production of TPAs is related to the IMF 1–2 hours (Kullen et al., 2002) or 3–4 hours (Fear and Milan, 2012) before the occurrence of a TPA. Here we use OMNI 1-minute-resolution solar wind data to study IMF B_z before TPA onset. Figure 4 shows the characteristics of IMF B_z before the occurrence of TPAs in each month. The four colored lines in the figure represent the characteristics of IMF B_z in this month 1, 2, 3, 4 hours before the appearance of each TPA (the start time and the end time of a TPA event are moved forward simultaneously, so that the time used to calculate IMF B_z is equal to the duration of TPA). They are calculated from the OMNI 1-minute-resolution solar wind data; the northward and southward IMF are calculated separately. The dotted black line (presenting background values) is calculated based on all the OMNI 1-hour-resolution solar wind data from 1996 to 2005 (corresponding to the times of the IMAGE and Polar satellite data), reflecting the long-term characteristics of IMF B_z.

Figure 4a shows the monthly binned average of IMF B_z prior to each TPA; Figure 4b shows the probabilities of IMF $B_z > 2$ nT and $B_z < -2$ nT before the occurrence of each TPA. These two figures show similar characteristics; that is, for southward IMF, the IMF B_z before each TPA is almost the same as the background value (dotted black line), but for the northward IMF, the IMF B_z before TPA is about twice the background value, which is consistent with previous research results. In other words, TPAs are more likely to occur when conditions are dominated by northward IMF with strong northward B_z components (Berkey et al., 1976; Gussenhoven, 1982; Kullen et al., 2002). Figure 4c shows the percentage of time allocated between the north and south directions of the IMF B_z before the TPA occurs. The upper part of the figure presents northward IMF ($B_z > 0$ nT); the lower part shows the southward IMF ($B_z < 0$ nT). It is clear from the figure that the northward IMF is more likely to be observed before the occurrence of a TPA, confirming again that the preferred condition for occurrence of TPAs

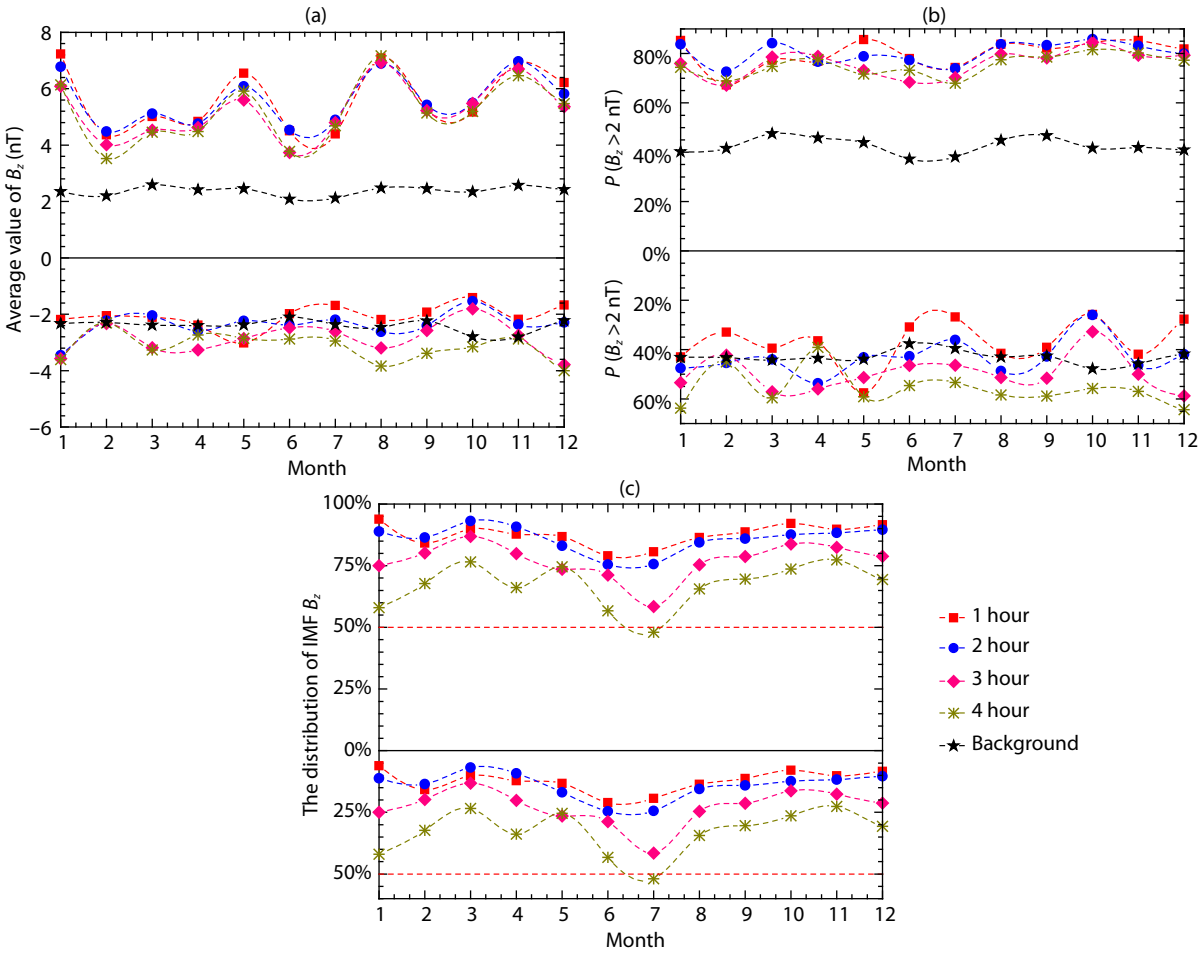

Figure 4. Here we use OMNI 1 minute resolution solar wind data to study IMF B_z before TPA onset. The time used to calculate IMF B_z is equal to the duration of TPA. (a) The average value of the IMF B_z for 1, 2, 3, 4 hours before the occurrence of TPA using 1min resolution IMNI data; the dotted black line indicates the background value (long-term average value of B_z). (b) Probability of IMF $B_z > 2$ nT and $B_z < -2$ nT for 1, 2, 3, 4 hours before TPA occurs; the dotted black line indicates the background value of probability of IMF $B_z > 2$ nT and $B_z < -2$ nT. The curves in the upper and the lower parts of both (a) and (b) correspond to the northward and southward IMF circumstances, respectively. (c) The percentage of time allocated between the north (upper) and south (lower) sides of the IMF B_z for 1, 2, 3, 4 hours before the TPA occurred. The dotted red line reflects the proportion of southward or northward IMF that is 50 percent.

is a solar wind dominated by the northward IMF B_z.

As can be seen from Figure 4a, the northward component of IMF before a TPA is generally larger than 2 nT, while the average value of the southward component is basically around 2 nT. This indicates that a TPA is more likely to occur when the northward component exceeds 2 nT. It is for this reason that we chose the value of 2 nT as a threshold to produce Figures 3b and 3d.

4. Summary and Discussion

In this study, we have used aurora data from appropriate auroral imaging satellites (IMAGE and Polar) and solar wind data from OMNI satellites for a statistical analysis of semi-annual variation in occurrence of transpolar arcs. We identify 532 TPA events, of which 437 occurred in the northern hemisphere and 95 in the southern hemisphere, and find that the incidence of TPAs is subject to a clear, systematic semiannual variation. A statistical analysis of the B_z component reveals that the ensemble average value of IMF B_z per month also exhibits a semiannual variation. The incidence of TPAs appears to have two peaks in the second half of the year, that is, September and November, but on the whole, TPA incidence shows a semiannual variation. From 1996 to 2005, the value of B_z exhibited a second, November, peak in the second half of the year. As we can see from Figure 4 the northward component of IMF B_z is dominant, and the amplitude is on average larger than that of the background before the occurrence of each TPA. Comparing the long term variation of TPA incidence and IMF, we find that the incidence of TPAs is related to the polarity and amplitude of the B_z component, which is consistent with the previous research results (Berkey et al., 1976; Gussenhoven, 1982; Kullen et al., 2002).

Although the R-M effect is a hypothesis to explain the semiannual variation of geomagnetic activity under southward IMF conditions, our analysis shows that it can also predict the semiannual variation of the northward IMF. Since the occurrence of TPAs is related to the amplitude of the northward B_z, it follows logically that the semiannual variation in the incidence of TPAs may be related

to the R-M effect.

In summary, we suggest that the semiannual variation of the TPA incidence may be related to the R-M effect. Consistent with the R-M effect, both the northward IMF B_z component and the incidence of TPAs appear follow a similar 6-month cycle; however, disagreement appears in November between the incidence of TPAs/IMF B_z and the prediction of the R-M effect. This anomaly will be further investigated in the future.

Acknowledgments

We acknowledge use of OMNI data obtained from the OMNIWeb service at http://omniweb.gsfc.nasa.gov. We thank the Polar UVI team for providing UV images. The IMAGE FUV data were provided by the NASA Space Science Data Center (NSSDC). This work was supported by the National Natural Science Foundation of China (Grants 41961130382, 41731068 and 41941001), the Royal Society NAF\R1\191047, International Space Science Institute (ISSI), and the young scholar plan of Shandong University at Weihai (2017WHWLJH08).

References

Bai, S. C., Shi, Q. Q., Tian, A. M., Nowada, M., Degeling, A. W., Zhou, X. Z., Zong, Q. G., Rae, I. J., Fu, S. Y., … Fazakerly, A. N. (2018). Spatial distribution and semiannual variation of cold-dense plasma sheet. *J. Geophys. Res. Space Phys.*, *123*(1), 464–472. https://doi.org/10.1002/2017JA024565

Berkey, F. T., Cogger, L. L., Ismail, S., and Kamide, Y. (1976). Evidence for a correlation between Sun-aligned arcs and the interplanetary magnetic field direction. *Geophys. Res. Lett.*, *3*(3), 145–147. https://doi.org/10.1029/GL003i003p00145

Carter, J. A., Milan, S. E., Fear, R. C., Walach, M. T., Harrison, Z. A., Paxton, L. J., and Hubert, B. (2017). Transpolar arcs observed simultaneously in both hemispheres. *J. Geophys. Res. Space Phys.*, *122*(6), 6107–6120. https://doi.org/10.1002/2016JA023830

Cliver, E. W., Kamide, Y., and Ling, A. G. (2000). Mountains versus valleys: Semiannual variation of geomagnetic activity. *J. Geophys. Res. Space Phys.*, *105*(A2), 2413–2424. https://doi.org/10.1029/1999JA900439

Cliver, E. W., Kamide, Y., and Ling, A. G. (2002). The semiannual variation of geomagnetic activity: phases and profiles for 130 years of aa data. *J. Atmos. Sol. Terr. Phys.*, *64*(1), 47–53. https://doi.org/10.1016/S1364-6826(01)00093-1

Craven, J. D., Murphree, J. S., Frank, L. A., and Cogger, L. L. (1991). Simultaneous optical observations of transpolar arcs in the two polar caps. *Geophys. Res. Lett.*, *18*(12), 2297–2300. https://doi.org/10.1029/91GL02308

Crooker, N. U. (1992). Reverse convection. *J. Geophys. Res. Space Phys.*, *97*(A12), 19363–19372. https://doi.org/10.1029/92JA01532

Eriksson, S., Baker, J. B. H., Petrinec, S. M., Wang, H., Rich, F. J., Kuznetsova, M., Dunlop, M. W., Rème, H., Greenwald, R. A., … Carlson, C. W. (2005). On the generation of enhanced sunward convection and transpolar aurora in the high-latitude ionosphere by magnetic merging. *J. Geophys. Res. Space Phys.*, *110*(A11), A11218. https://doi.org/10.1029/2005JA011149

Fear, R. C., and Milan, S. E. (2012). The IMF dependence of the local time of transpolar arcs: Implications for formation mechanism. *J. Geophys. Res. Space Phys.*, *117*(A3), A03213. https://doi.org/10.1029/2011JA017209

Feldstein, Y. I., and Starkov, G. V. (1967). Dynamics of auroral belt and polar geomagnetic disturbances. *Planet. Space Sci.*, *15*(2), 209–229. https://doi.org/10.1016/0032-0633(67)90190-0

Frank, L. A., Craven, J. D., Burch, J. L., and Winningham, J. D. (1982). Polar views of the Earth's aurora with Dynamics Explorer. *Geophys. Res. Lett.*, *9*(9), 1001–1004. https://doi.org/10.1029/GL009i009p01001

Frank, L. A., Craven, J. D., and Rairden, R. L. (1985). Images of the earth's aurora and geocorona from the Dynamics Explorer Mission. *Adv. Space Res.*, *5*(4), 53–68. https://doi.org/10.1016/0273-1177(85)90116-4

Frank, L. A., Craven, J. D., Gurnett, D. A., Shawhan, S. D., Weimer, D. R., Burch, J. L., Winningham, J. D., Chappell, C. R., Waite, J. H., … Shelley, E. G. (1986). The theta aurora. *J. Geophys. Res. Space Phys.*, *91*(A3), 3177–3224. https://doi.org/10.1029/JA091iA03p03177

Gussenhoven, M. S. (1982). Extremely high latitude auroras. *J. Geophys. Res. Space Phys.*, *87*(A4), 2401–2412. https://doi.org/10.1029/JA087iA04p02401

Gussenhoven, M. S., and Mullen, E. G. (1989). Simultaneous relativistic electron and auroral particle access to the polar caps during interplanetary magnetic field B_z northward: A scenario for an open field line source of auroral particles. *J. Geophys. Res. Space Phys.*, *94*(A12), 17121–17132. https://doi.org/10.1029/JA094iA12p17121

Hultqvist, B. (1974). Rocket and satellite observations of energetic particle precipitation in relation to optical aurora. *Ann. Geophys.*, *30*(2), 223–257.

Kullen, A. (2000). The connection between transpolar arcs and magnetotail rotation. *Geophys. Res. Lett.*, *27*(1), 73–76. https://doi.org/10.1029/1999GL010675

Kullen, A., Brittnacher, M., Cumnock, J. A., and Blomberg, L. G. (2002). Solar wind dependence of the occurrence and motion of polar auroral arcs: A statistical study. *J. Geophys. Res. Space Phys.*, *107*(A11), 13-1–13-23. https://doi.org/10.1029/2002JA009245

Kullen, A. (2012). Transpolar arcs: Summary and recent results. In A. Keiling, et al. (Eds.), *Auroral Phenomenology and Magnetospheric Processes: Earth And Other Planets* (pp. 69-80). Washington: AGU. https://doi.org/10.1029/2011GM001183

Lassen, K., and Danielsen, C. (1989). Distribution of auroral arcs during quiet geomagnetic conditions. *J. Geophys. Res. Space Phys.*, *94*(A3), 2587–2594. https://doi.org/10.1029/JA094iA03p02587

Li, X., Ramachandran, R., Movva, S., Graves, S., Germany, G., Lyatsky, W., and Tan, A. (2004). Dayglow removal from FUV auroral images. In *2004 IEEE International Geoscience and Remote Sensing Symposium* (pp. 3774–3777). Anchorage, AK: IEEE. https://doi.org/10.1109/IGARSS.2004.1369944

Liou, K., Newell, P. T., Sibeck, D. G., Meng, C. I., Brittnacher, M., and Parks, G. (2001). Observation of IMF and seasonal effects in the location of auroral substorm onset. *J. Geophys. Res. Space Phys.*, *106*(A4), 5799–5810. https://doi.org/10.1029/2000JA003001

Mailyan, B., Shi, Q. Q., Kullen, A., Maggiolo, R., Zhang, Y., Fear, R. C., Zong, Q. G., Fu, S. Y., Gou, X. C., … Pu, Z. Y. (2015). Transpolar arc observation after solar wind entry into the high-latitude magnetosphere. *J. Geophys. Res. Space Phys.*, *120*(5), 3525–3534. https://doi.org/10.1002/2014JA020912

Mende, S. B., Heetderks, H., Frey, H. U., Lampton, M., Geller, S. P., Habraken, S., Renotte, E., Jamar, C., Rochus, P., … Cogger, L. (2000a). Far ultraviolet imaging from the IMAGE spacecraft. 1. System design. *Space Sci. Rev.*, *91*(1-2), 243–270. https://doi.org/10.1023/A:1005271728567

Mende, S. B., Heetderks, H., Frey, H. U., Lampton, M., Geller, S. P., Abiad, R., Siegmund, O. H. W., Tremsin, A. S., Spann, J., … Trondsen, T. (2000b). Far ultraviolet imaging from the IMAGE spacecraft. 2. Wideband FUV imaging. *Space Sci. Rev.*, *91*(1-2), 271–285. https://doi.org/10.1023/A:1005227915363

Mende, S. B., Heetderks, H., Frey, H. U., Stock, J. M., Lampton, M., Geller, S. P., Abiad, R., Siegmund, O. H. W., Habraken, S., … Lauche, H. (2000c). Far ultraviolet imaging from the IMAGE spacecraft. 3. Spectral imaging of Lyman-α and OI 135.6 nm. *Space Sci. Rev.*, *91*(1-2), 287–318.

Milan, S. E., Hubert, B., and Grocott, A. (2005). Formation and motion of a transpolar arc in response to dayside and nightside reconnection. *J. Geophys. Res. Space Phys.*, *110*(A1), A01212. https://doi.org/10.1029/2004JA010835

Peterson, W. K., and Shelley, E. G. (1984). Origin of the plasma in a cross-polar cap auroral feature (theta aurora). *J. Geophys. Res. Space Phys.*, *89*(A8), 6729–6736. https://doi.org/10.1029/JA089iA08p06729

Rees, M. H. (1963). Auroral ionization and excitation by incident energetic electrons. *Planet. Space Sci.*, *11*(10), 1209–1218. https://doi.org/10.1016/0032-0633(63)90252-6

Russell, C. T., and McPherron, R. L. (1973). Semiannual variation of geomagnetic activity. *J. Geophys. Res.*, *78*(1), 92–108. https://doi.org/10.1029/JA078i001p00092

Shi, Q. Q., Zong, Q. G., Zhang, H., Pu, Z. Y., Fu, S. Y., Xie, L., Wang, Y. F., Chen, Y., Li, L., … Lucek, E. (2009). Cluster observations of the entry layer

equatorward of the cusp under northward interplanetary magnetic field. *J. Geophys. Res. Space Phys.*, *114*(A12), A12219. https://doi.org/10.1029/2009JA014475

Shi, Q. Q., Zong, Q. G., Fu, S. Y., Dunlop, M. W., Pu, Z. Y., Parks, G. K., Wei, Y., Li, W. H., Zhang, H., … Lucek, E. (2013). Solar wind entry into the high-latitude terrestrial magnetosphere during geomagnetically quiet times. *Nat. Commun.*, *4*, 1466. https://doi.org/10.1038/ncomms2476

Tanaka, T., Obara, T., and Kunitake, M. (2004). Formation of the theta aurora by a transient convection during northward interplanetary magnetic field. *J. Geophys. Res. Space Phys.*, *109*(A9), A09201. https://doi.org/10.1029/2003JA010271

Torr, M. R., Torr, D. G., Zukic, M., Johnson, R. B., Ajello, J., Banks, P., Clark, K., Cole, K., Keffer, C., … Spann, J. (1995). A far ultraviolet imager for the International Solar-Terrestrial Physics Mission. *Space Sci. Rev.*, *71*(1-4), 329–383. https://doi.org/10.1007/BF00751335

Yokoyama, N., Kamide, Y., and Miyaoka, H. (1998). The size of the auroral belt during magnetic storms. *Ann. Geophys.*, *16*(5), 566–573. https://doi.org/10.1007/s00585-998-0566-z

Yue, C., Zong, Q. G., Zhang, H., Wang, Y. F., Yuan, C. J., Pu, Z. Y., Fu, S. Y., Lui, A. T. Y., Yang, B., and Wang, C. R. (2010). Geomagnetic activity triggered by interplanetary shocks. *J. Geophys. Res. Space Phys.*, *115*(A5), A00105. https://doi.org/10.1029/2010JA015356

Yue, C., and Zong, Q. G. (2011). Solar wind parameters and geomagnetic indices for four different interplanetary shock/ICME structures. *J. Geophys. Res. Space Phys.*, *116*(A12), A12201. https://doi.org/10.1029/2011JA017013

Yue, C., Zong, Q. G, Wang, Y. F., Vogiatzis, I. I., Pu, Z. Y., Fu, S. Y., and Shi, Q. Q. (2011). Inner magnetosphere plasma characteristics in response to interplanetary shock impacts. *J. Geophys. Res. Space Phys.*, *116*(A11), A11206. https://doi.org/10.1029/2011JA016736

Zhang, X. Y., Zong, Q. G., Wang, Y. F., Zhang, H., Xie, L., Fu, S. Y., Yuan, C. J., Yue, C., Yang, B., and Pu, Z. Y. (2010). ULF waves excited by negative/positive solar wind dynamic pressure impulses at geosynchronous orbit. *J. Geophys. Res. Space Phys.*, *115*(A10), A10221. https://doi.org/10.1029/2009JA015016

Zhao, H., and Zong, Q. G. (2012). Seasonal and diurnal variation of geomagnetic activity: Russell–McPherron effect during different IMF polarity and/or extreme solar wind conditions. *J. Geophys. Res. Space Phys.*, *117*(A11), A11222. https://doi.org/10.1029/2012JA017845

Zhou, X. Z., Ge, Y. S., Angelopoulos, V., Runov, A., Liang, J., Xing, X., Raeder, J., and Zong, Q. G. (2012). Dipolarization fronts and associated auroral activities: 2. Acceleration of ions and their subsequent behavior. *J. Geophys. Res. Space Phys.*, *117*(A10), A10227. https://doi.org/10.1029/2012JA017677

Zong, Q.-G., Zhou, X.-Z., Wang, Y. F., Li, X., Song, P., Baker, D. N., Fritz, T. A., Daly, P. W., Dunlop, M., and Pedersen, A. (2009). Energetic electron response to ULF waves induced by interplanetary shocks in the outer radiation belt. *J. Geophys. Res. Space Phys.*, *114*(A10), A10204. https://doi.org/10.1029/2009JA014393

Zong, Q.-G., Wang, Y. F., Zhang, H., Fu, S. Y., Zhang, H., Wang, C. R., Yuan, C. J., and Vogiatzis, I. (2012). Fast acceleration of inner magnetospheric hydrogen and oxygen ions by shock induced ULF waves. *J. Geophys. Res. Space Phys.*, *117*(A11), A11206. https://doi.org/10.1029/2012JA018024